

# Clinically Important Characteristics of Maximum-Likelihood Reconstruction

Tom R. Miller and Jerold W. Wallis

*The Edward Mallinckrodt Institute of Radiology, Washington University School of Medicine, St. Louis, Missouri*

SPECT images of a Jaszczak rod phantom, a single-slice Hoffman brain phantom and a uniform water-bath were acquired. Simulated noisy bar phantoms incorporating depth-dependent attenuation and blur were produced and compared to simulations with depth-independent attenuation and blur, as is the case in PET. Following iterative maximum-likelihood reconstruction, regularization was performed with use of Gaussian filters. While correction for attenuation is achieved in approximately 10 iterations, spatial resolution in the SPECT reconstructions, quantified by contrast in the bar simulations and by visual inspection of the real data, was highly nonuniform, being poorest at the center and improving toward the periphery. Image resolution continued to improve well beyond 50 iterations when regularization was applied that maintained a constant signal-to-noise ratio. Contrast in the simulated PET data also improved with increasing iterations, but the PET data showed uniform contrast throughout the transaxial slices at all numbers of iterations.

**J Nucl Med 1992; 33:1678-1684**

There is increasing interest in maximum-likelihood reconstruction in single-photon emission computed-tomography (SPECT) (1-4) and positron-emission tomography (PET) (5,6). In SPECT imaging, maximum-likelihood reconstruction may improve quantification (2) and yield more accurate attenuation compensation, especially in the chest (1,7). This reconstruction technique also shows promise in PET imaging of the brain (6).

Despite this widespread interest in maximum-likelihood reconstruction, there have been few systematic, quantitative studies of fundamental properties of the algorithm in tomographic reconstruction (8). This paper addresses the following questions:

1. Are attenuation and resolution in reconstructed slices uniform across the slice?
2. How many iterations of the algorithm are required? Is there an optimum number of iterations?
3. Are the resolution characteristics the same in SPECT and PET imaging?

We believe the answers to all of these questions have important clinical implications.

## METHODS

### The Expectation-Maximization Algorithm for Maximum-Likelihood Reconstruction

The basic concept of maximum-likelihood reconstruction is simple: the activity distribution in the reconstructed slice is chosen to be the one with the "maximum likelihood" of producing the observed projection data. Since no analytic solution is available, the reconstruction must be performed iteratively, usually with use of the expectation-maximization algorithm. Two equations for the iterative expectation-maximization calculation are in wide use (3,9). They differ only in choice of the "complete data," and they converge to the same final solution. The equation proposed by Lange and Carson (9) will be used here because it appears to converge faster than the other algorithm (6).

### The "Noise" Problem with Increasing Iterations

As the number of iterations of the expectation-maximization algorithm increases, the reconstructed images become increasingly "noisy." This undesirable phenomenon has led several authors to propose stopping at 50 iterations (2,10,11). Some have suggested continuing to iterate, believing the reconstructed image will improve rather than deteriorate if appropriate constraints are applied. Several constraint techniques have been proposed (12-17). In this paper, the data will be presented both without constraints or regularization and with post-iteration Gaussian regularization based upon the "method of sieves" (12,13). The Gaussian filters were implemented as  $15 \times 15$  pixel convolution filters applied to the reconstructed slices after iteration (18).

### Differences Between SPECT and PET Reconstruction

In maximum-likelihood reconstruction, the physics of the imaging situation is explicitly included in the projection and backprojection steps. In SPECT imaging, the spatial resolution and photon attenuation are both strongly dependent upon depth (19). In PET, resolution is almost completely independent of depth, and attenuation is usually considered to be constant along any particular reconstruction ray or cylinder with the attenuation values based on a transmission measurement (19). Thus, while the superficial form of the iterative equations for SPECT and PET appear identical, the projection and backprojection operators are fundamentally different.

### Experimental Image Data

Two sets of experimental data were acquired. One was from a Jaszczak phantom (Data Spectrum Corp., Chapel Hill, NC) filled with 20 mCi  $^{99m}\text{Tc}$ . Half of the phantom contained only radio-

Received Jan. 30, 1992; accepted Apr. 13, 1992.  
For reprints contact: Tom R. Miller, MD, PhD, The Edward Mallinckrodt Institute of Radiology, 510 S. Kingshighway Blvd., St. Louis, MO 63110.

active water, while the other half contained six sets of rods with diameters from 4.8 to 12.7 mm. The other study was of a single-slice Hoffman brain phantom (20) filled with 3 mCi  $^{99m}\text{Tc}$ . Both studies were collected on a single-head rotating gamma camera (Siemens Orbiter, Siemens Medical Systems, Hoffman Estates, IL) equipped with a high-resolution collimator. Data were collected in a  $128 \times 128$  pixel matrix at 90 angles over  $360^\circ$ . Pixel dimension was  $3.1 \times 3.1$  mm. Several rows of projection data were summed before reconstruction in the Jaszczak study to give high-count, low-noise slices. Three rows were summed in the Hoffman phantom to account for the 9 mm thickness of the phantom. The dimensions of the phantoms, total projection counts and radius of rotation are given in Table 1. To speed reconstruction, the central  $80 \times 80$  pixels of the projection data were used for the Jaszczak study and  $64 \times 64$  pixels were used for the Hoffman data; the phantoms were centered on the axis of rotation to avoid missing projection data.

### Simulated Image Data

Four very simple computer-simulated phantoms were created to assess the uniformity of spatial resolution (Table 1). The phantoms were created with the same pixel dimensions and matrix sizes as used with the experimental data. The first two phantoms were in a cross-hatch pattern with bar thicknesses of 4 or 3 pixels and dimensions typical of body and head imaging. The spaces between the bars were of the same thickness and contained zero counts. The third and fourth phantoms consisted of 4-pixel or 3-pixel vertical bars with spaces containing 50% of the activity in the bars. The "body" phantoms were produced with diameters equal to the Jaszczak phantom, while the "head" phantoms were designed with the dimensions of the Hoffman phantom. These simulated phantoms were rotated through 90 angles over  $360^\circ$  and projected with use of the collimator resolution-function and attenuation values described below. The total counts and radius of rotation for the larger (body) phantoms were chosen to correspond to typical values for a clinical study of the abdomen with a triple-head camera. Values for the smaller (head) phantoms were similar to those in a brain study with a triple-head camera. Poisson noise was added with use of a random number generator.

For SPECT imaging, the depth-dependent spatial resolution of the gamma-camera was measured by planar imaging of a line source filled with  $^{99m}\text{Tc}$  imbedded in a lucite scattering medium.

The resolution, assumed to be Gaussian in shape, was characterized as a function of depth,  $D$  (cm), by the full width at half maximum (FWHM) according to the following equation:

$$\text{FWHM (cm)} = \sqrt{(0.47)^2 + (0.056D)^2}$$

A linear attenuation coefficient of 0.13/cm was used for the SPECT simulations; a value of 0.15/cm resulted in negligible differences in the results.

To approximate the acquisition characteristics of PET imaging, simulated data were also generated with a constant resolution of 8 mm FWHM and a constant attenuation value of 0.096/cm (19).

### Implementation of the Iterative Reconstruction

The iterative reconstruction algorithm was implemented for parallel projection and backprojection rays as would be obtained with use of a parallel-hole collimator. The computations were performed on a modern reduced-instruction-set (RISC) workstation (DECstation 5000/200, Digital Equipment Corp., Maynard, MA). Each iteration of the algorithm required only 7–12 sec with use of an approach we have developed (21) that involves one precomputation of the projection and backprojection operators requiring less than 100 sec with subsequent storage in computer memory; at each iteration only a table lookup is then required followed by simple floating-point calculations.

### Data Analysis

The real experimental data were used to analyze quantitatively the attenuation compensation and evaluate qualitatively the depth-dependence of resolution and the performance of the algorithm with increasing numbers of iterations. The spatial resolution was analyzed with use of the simulated phantoms. The simulated data from the 3- and 4-pixel vertical bars were used to quantify the depth-dependence of resolution. Because of the edge artifact present in maximum-likelihood reconstruction (12,13), a measure of contrast between the bars and spaces was employed rather than a measure such as the point spread function that would be more prone to artifactual results. The counts within the full width of the central bar ( $C_{\text{bar}}$ ) were summed at the center of the circular phantom and at one-half of the distance to the edge of the phantom. The counts in the space between the bars were similarly determined ( $C_{\text{space}}$ ). The contrast at the center and at the mid-radius was then computed as  $(C_{\text{bar}} - C_{\text{space}})/C_{\text{bar}}$ . The ideal

TABLE 1  
Characteristics of the Real and Simulated Phantoms

Phantom	Type	Diameter (cm)	Total projection counts	Radius of rotation (cm)	Figure
Jaszczak—uniform	Real	21.6	1,750,000	19	1
Jaszczak—rods	Real	21.6	2,870,000	19	7
Hoffman brain	Real	$16 \times 12$ (oval)	212,000	15	8
Cross-hatch (4 pixel)—body	Simulated	21.7	$\infty^*$	25	2
Cross-hatch (3 pixel)—head	Simulated	16.1	$\infty$	15	3
Vertical bars (4 pixel)—body	Simulated	21.7	500,000	25	4
			or $\infty$		
Vertical bars (3 pixel)—head	Simulated	16.1	600,000	15	—
			or $\infty$		

\* Noise-free.

contrast of the phantoms was 0.5. Results are expressed as a fraction of the ideal contrast.

When regularization is employed to compensate for the "noise" artifact, the resolution of the Gaussian regularizer should be selected in a rational manner. We selected the regularizing filter so that the signal-to-noise ratio (SNR) in the reconstructed slice after regularization would be constant as the number of iterations increased. The SNR of the image after 50 iterations without regularization was selected because several authors have proposed performing maximum-likelihood reconstruction with that number of iterations and no regularization (2,10,11). To determine the SNR for the simulated data, 25 realizations of the projection data were created with the use of a random-number generator. Reconstructions then were performed separately for each projection set, leading to 25 noisy slices from each phantom. The SNR for each phantom was then computed on a pixel-by-pixel basis as the mean of the 25 images divided by the standard deviation. Mean and SNR images were then created. The average SNR was computed from the SNR image within the phantom except for the 5 pixels closest to the periphery where there could be edge artifact.

It was not practical to collect the identical experimental phantom data 25 times because of the very long total acquisition time and the declining counting rate caused by radioactive decay. Thus, the SNR was estimated from an annulus in the uniform section of the Jaszczak phantom. Within an annulus of the symmetric phantom, the mean counts will be constant and the variance of the counts will be uniform. An annulus was chosen rather than the entire phantom to avoid potential problems with imperfect attenuation compensation and nonuniform distribution of noise. Thus, the mean and standard deviation of the pixel counts in a 5-pixel thick annulus at one-half of the phantom radius were determined and the SNR was computed as the mean of the counts in the annulus divided by the standard deviation.

## RESULTS

Figure 1 shows a profile through the center of the uniform "water bath" section of the Jaszczak phantom after 10 iterations. The essentially flat shape of the profile

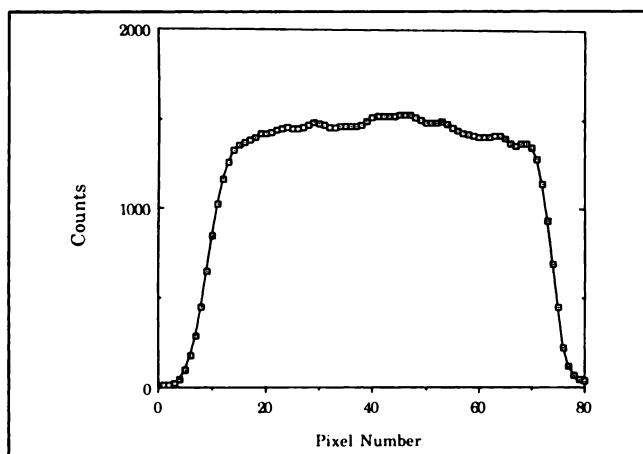


**FIGURE 1.** The counts in a cross-sectional slice through the center of the water bath section of the Jaszczak phantom is shown after 10 iterations of the maximum-likelihood algorithm without regularization.

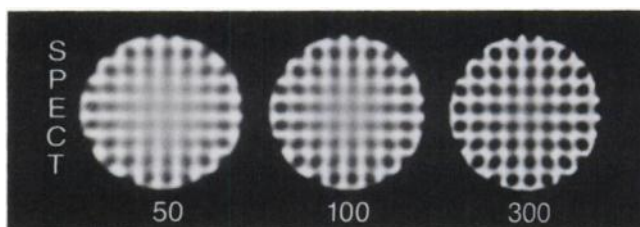


**FIGURE 2.** The simulated, noise-free cross-hatch phantom is shown for SPECT imaging with dimensions typical of body acquisition. Reconstructions are shown after 50, 100 and 300 iterations.

did not change with larger numbers of iterations except for the well-known increase in the noise and edge artifacts (12,13). Thus, only 10 iterations are required to achieve complete attenuation compensation with this uniform attenuating medium.

Figures 2 and 3 show reconstructions of the cross-hatch simulated, noise-free phantom for dimensions characteristic of both body and brain SPECT imaging and for the PET-like situation. This phantom, illustrating resolution, demonstrates that for SPECT imaging resolution is poorer at the center of the image than closer to the periphery. The relative resolution at the center compared to periphery improves with increasing number of iterations. Resolution is independent of depth for the PET-like simulation. This phenomenon is quantified with use of the noise-free vertical bar phantoms shown in Figure 4 for body imaging with SPECT and the similar phantoms, not shown, for the head and PET cases. The noise-free bars were used for analysis; the results were essentially the same, but more variable, when the noisy bars were used. As described above, regularization was not performed at 50 iterations. Gaussian regularizers were chosen for higher iterations to give a SNR equal to that at 50 iterations. For the images in Figure 4, the FWHM of the Gaussian

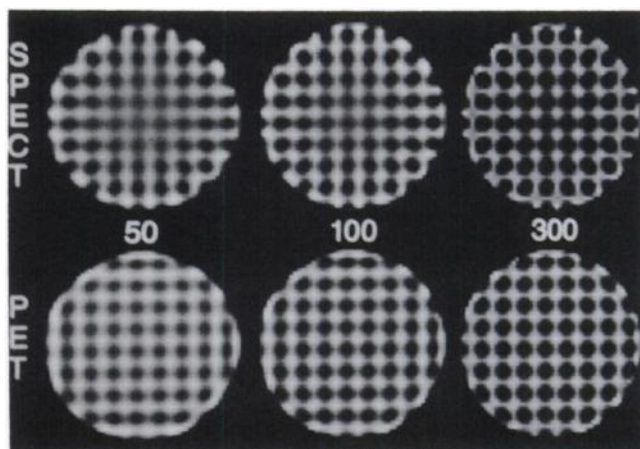


**FIGURE 3.** The upper row shows the cross-hatch phantom for a simulated SPECT study with dimensions typical of head imaging. The lower row shows the same phantom, but with imaging similar to the PET case. Reconstructions are shown after 50, 100 and 300 iterations.

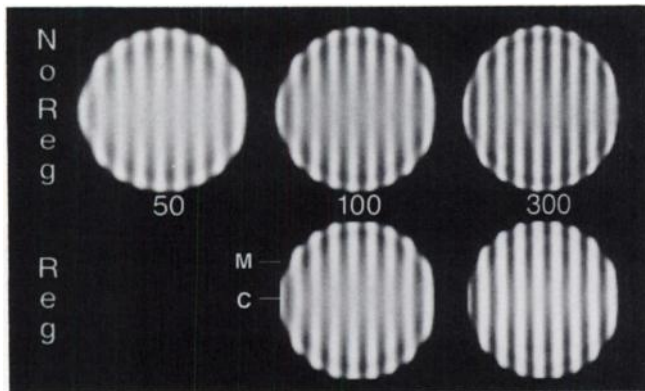


**FIGURE 4.** The vertical bar phantom is shown for simulated SPECT imaging with body dimensions. The upper row shows reconstructions for 50, 100 and 300 iterations without regularization. The lower row shows images after 100 and 300 iterations with Gaussian regularization. The marks labeled "C" and "M" represent the position of the horizontal profiles used to compute contrast at the center and mid-radius of the phantom. The slight truncation at the upper and right edges is related to the size of the convolution filter mask.

regularizers was 9.1 and 12.5 mm for the images at 100 and 300 iterations, respectively.

Figures 5 and 6 are data derived from the vertical bar phantoms. They show the ratio of the contrast at the center of the images and half-way to the edge compared to the ideal contrast of 0.5 for the large and small phantoms representing body and head SPECT imaging with and without regularization. Note the gradual improvement in contrast with number of iterations and the inferior contrast at the center of the images. The relative and absolute differences between the center and mid-radius contrast decreased with increasing numbers of iterations. The slight fall in contrast after regularization at the mid-radius for the head situation at 250 and 300 iterations is due to

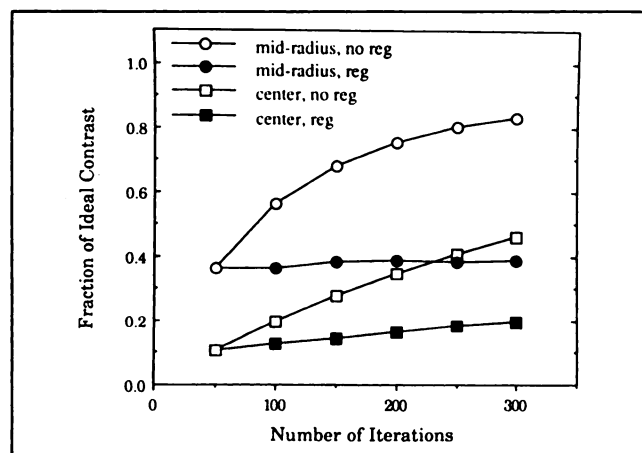


**FIGURE 5.** The ratio of the measured contrast to the ideal contrast of 0.5 is shown for SPECT imaging of the simulated vertical bar phantoms with body dimensions. Data are shown at the center of the phantom and half-way to the periphery with and without regularization.

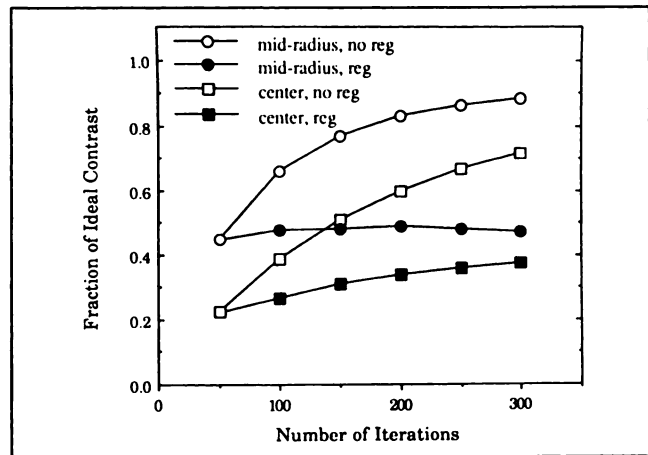


**FIGURE 6.** The contrast ratios for simulated head SPECT imaging are shown in the same format as in Figure 5.

increasing smoothness of the Gaussian regularizers, as discussed more fully below. Results for the vertical bar PET-like situation showed average contrast ratios without regularization rising from 0.41 at 50 iterations to 0.87 at 300 iterations. Values differed between the center and mid-radius by only 0.03 at 50 iterations and 0.01 at 300 iterations.

The SNR was slightly lower at the center of the simulated SPECT images than at the periphery. Since the algorithm accurately compensates for attenuation, the mean value is contrast, thus indicating that there is greater noise at the image center. This variation is caused by depth-dependent attenuation leading to fewer detected counts coming from the center of the image.

To verify the quantitative SPECT results achieved with the simulated bar phantoms, the experimental Jaszczak and Hoffman data were reconstructed for 50, 300 and 1000 iterations, as shown in Figures 7 and 8. Regularization was applied at 300 and 1000 iterations. The regularizer for the Jaszczak phantom at 300 iterations (10.1 mm

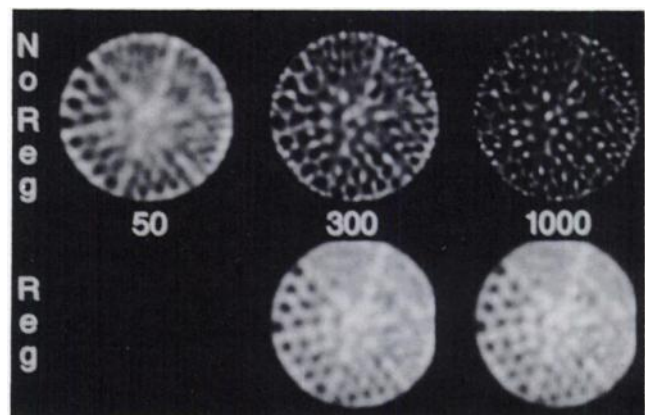


**FIGURE 7.** Reconstructions through the rod section of the Jaszczak phantom are shown after 50, 300 and 1000 iterations. The upper row is without regularization, while the lower row shows reconstructions at 300 and 1000 iterations with Gaussian regularization.



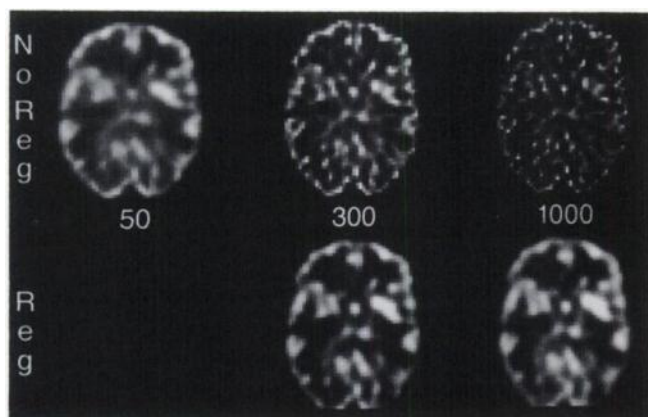


**FIGURE 8.** The Hoffman brain phantom is shown after 50, 300 and 1000 iterations. The format is the same as in Figure 7.

FWHM) was chosen to give a constant SNR in a mid-annulus as described above. For the Hoffman phantom and for the Jaszczak phantom at 1000 iterations, the regularizers were selected to give clinically acceptable and visually similar noise levels. Note that resolution at the center of the phantoms is inferior to that at the periphery, especially at low iteration numbers, and the resolution in the center plateaus or continues to improve after regularization, even at 1000 iterations, thus confirming the simulated results in Figures 5 and 6. The center of the Jaszczak phantom is noisier than the more peripheral regions, although that phenomenon is difficult to appreciate in photographic reproductions of the images.

## DISCUSSION

There are several principal conclusions to be drawn from this work.

1. **Attenuation Compensation.** Accurate attenuation compensation for a uniform attenuation medium is achieved after approximately 10 iterations (Fig. 1).
2. **Resolution.** Spatial resolution in SPECT reconstruction is variable across the slice, being the worst in the center and becoming more uniform with increasing number of iterations (Figs. 2–8). To our knowledge, this fact has not previously been reported.
3. **Number of Iterations.** The reconstructed images continue to improve in quality (improving spatial resolution at a constant SNR) well beyond 50 iterations with plateauing or a possible slight decline at large numbers of iterations (Figs. 2–8). This issue, a very controversial topic for many years, will be discussed further below.
4. **PET.** The depth dependence of resolution observed with SPECT may not be present in PET imaging (Fig. 3 and data in the Results).

## Methodological Issues

Quantification of the spatial resolution in maximum-likelihood reconstruction is a difficult issue. Ideally, point

sources would be employed with results expressed in terms of the measured full-width half-maximum. Unfortunately, many filtering and reconstruction techniques, including, among others, filtering of planar images with sharp filters such as the Wiener filter, and maximum-likelihood reconstruction, produce artifactual enhancement of object edges. Thus, the FWHM of a point source would become artifactually narrow and, thus, no longer representative of the ability to distinguish adjacent structures. For this reason we have chosen to use a bar pattern simulation and indirectly quantify “resolution” by a contrast measure. The Jaszczak and Hoffman phantoms are evaluated in a more subjective, visual way.

The SNR is an important measure of image quality that is closely related to resolution. Differing reconstruction factors, including the choice of filter in filtered backprojection and the regularizer in maximum-likelihood, lead to widely varying and inversely related resolution and noise. Therefore, to simplify analysis of the results, we have chosen to hold the SNR constant as iteration number increases and measure the changing contrast. Similarly, contrast or another measure related to resolution could be fixed and noise change could be quantified.

Scatter correction has not been employed in either the simulations or reconstructions. While the Hoffman phantom is very thin with negligible scatter, the images obtained from the rod section of the Jaszczak phantom (Fig. 7) are degraded by scatter, thus reducing overall image contrast. If scatter correction were applied, e.g., with dual-window correction of the projection data (22), the enhanced contrast might make the depth-dependence of the spatial resolution more apparent. However, correction for scatter would not change the principal conclusions of this work.

## Number of Iterations

Many workers now perform maximum-likelihood reconstructions with 50 iterations (2,10,11), believing either that the increasing noise with further iterations leads to deterioration of the images or that no gains will arise with further time-consuming iterations. The results reported here showing that spatial resolution is nonuniform and that image quality improves beyond 50 iterations suggest that more iterations should be employed. In fact, excellent reconstructions are obtained with the computationally impractical number of 1000 iterations (Figs. 7–8).

There may be an optimum number of iterations. As shown in Figures 5 and 6, the contrast at the mid-radius plateaus or falls slightly at 300 iterations when a Gaussian regularizer is employed. This phenomenon is due to the increasingly smooth regularizers required to hold image noise constant as iteration number increases. If other regularization methods are employed, this feature of maximum-likelihood reconstruction may disappear, or an optimum number may occur at a different point.

It is likely that the appropriate number of iterations will depend upon the details of the imaging situation including the counting rate, organ dimensions, uniformity of the

attenuating medium, camera parameters and other factors. Thus, further experiments will be required, ultimately with clinical patient data, to fully answer this question for each imaging situation.

We have chosen to use unconstrained maximum-likelihood reconstruction with post-processing regularization by the kernel-sieve method (12,13). Other related techniques, such as maximum-likelihood with use of Good's roughness measure (23,24), Gibbs priors (14,16) or other related methods (15,17) might give superior results to those reported here. However, the fundamental conclusions of this work would not likely change.

### Computation Speed

A major factor affecting choice of iteration number is the time required to perform the computation-intensive iterations. Special multi-processor machines can perform single-slice iterations at a rate of 40–300 per minute (24, 25). It may also be possible to speed convergence of the iterative algorithm (26,27). As conventional workstations continue to improve in speed, clinically acceptable computation times may become a reality with the use of these widely available low-cost machines.

The slower resolution improvement in the image center suggests a simple modification to the iterative scheme to more efficiently use the computer time. As the iterations proceed, a progressively smaller area about the image center is backprojected at each iteration. Thus, iterations become faster with concentration on the region with the lowest resolution. While this concept will require further development that is beyond the scope of this paper, a single, preliminary trial was performed. After the first 150 iterations of the standard algorithm, 225 additional iterations were performed within a smoothly shrinking area, leading to a total of 375 iterations consuming the same time as the standard method with 300 iterations. Bar phantom contrast improved at the center with only slight loss peripherally compared to the standard method.

### SPECT Versus PET

There is a simple, intuitive explanation for the property of maximum-likelihood reconstruction that the resolution in the center of the slice lags behind the resolution at the periphery. Gamma-ray attenuation and depth-dependent collimator resolution in SPECT lead to fewer and more blurred detected photons in the projections coming from the center of the image than from the edges. Thus, the maximum-likelihood algorithm has more difficulty in selecting the correct activity distribution in the center of the object because the algorithm is dealing with smaller numbers of events that are spread over a larger area of the detector surface.

If the depth-dependence of attenuation and resolution is removed, as is approximately true in PET (19), then it is plausible to anticipate that the reconstructed slices would not show the depth-dependence in resolution observed in SPECT imaging. That appears to be the case in the simu-

lated "PET" results reported here (Fig. 3 and in the data in the Results). Further experimental verification of this observation will be required employing the proper fan-beam geometry and PET measurements of real phantoms.

### Clinical Implications

In clinical SPECT studies, information at the center of the reconstructed slice is generally as important as information at the periphery. Therefore, because of the depth-dependence of resolution, it is doubtful that 50 iterations of the maximum-likelihood algorithm (2,10,11) will be adequate to resolve clinically important small structures. This observation may not have been made previously because phantom studies usually have not specifically addressed resolution at the center.

To achieve the most accurate clinical interpretations by visual analysis of images, it is desirable to have the best possible spatial resolution and uniformity with minimum noise. The results presented here with real phantoms closely approximating clinical brain studies (Hoffman phantom) and more generally corresponding to abdominal studies (Jaszczak phantom) show that resolution improves at a constant noise level with increasing numbers of iterations. The images do not deteriorate as frequently suggested (2,10,11). While there are practical limits due to computation time and computer cost, it appears that more than 50 iterations will be needed to achieve worthwhile results with the maximum-likelihood algorithm. Other, more complex "regularization" methods (14–17,23,24) may give even better results than those reported here.

### ACKNOWLEDGMENTS

We are grateful to Drs. Donald L. Snyder and Michael I. Miller for their encouragement and advice.

### REFERENCES

1. Tsui BMW, Gullberg GT, Edgerton ER, et al. Correction of nonuniform attenuation in cardiac SPECT imaging. *J Nucl Med* 1989;30:497–507.
2. Gilland DR, Jaszczak RJ, Greer KL, Coleman RE. Quantitative SPECT reconstruction of iodine-123 data. *J Nucl Med* 1991;32:527–533.
3. Miller MI, Snyder DL, Miller TR. Maximum-likelihood reconstruction for single-photon emission computed tomography. *IEEE Trans Nucl Sci* 1985;NS-32:769–778.
4. Chornoboy ES, Chen CJ, Miller MI, Miller TR, Snyder DL. An evaluation of maximum likelihood reconstruction for SPECT. *IEEE Trans Med Imaging* 1990;9:99–110.
5. Shepp LA, Vardi Y. Maximum likelihood reconstruction for emission tomography. *IEEE Trans Med Imaging* 1982;MI-1:113–122.
6. Polite DG, Snyder DL. Corrections for accidental coincidences and attenuation in maximum-likelihood image reconstruction for positron-emission tomography. *IEEE Trans Med Imaging* 1991;10:82–99.
7. Gullberg GT, Christian PE, Gengsheng LZ, Datz FL, Morgan HT. Cone beam tomography of the heart using single-photon emission-computed tomography. *Invest Radiol* 1991;26:681–688.
8. Liow J, Strother SC. Practical tradeoffs between noise, quantitation, and number of iterations for maximum likelihood-based reconstructions. *IEEE Trans Med Imaging* 1991;10:563–571.
9. Lange K, Carson R. EM reconstruction algorithms for emission and transmission tomography. *J Comp Assist Tomogr* 1984;8:306–316.
10. Zeng GL, Gullberg GT, Tsui BMW, Terry JA. Three-dimensional iterative reconstruction algorithms with attenuation and geometric point response corrections. *IEEE Trans Nucl Sci* 1991;38:693–702.

11. Tourassi GD, Gloyd CE Jr, Munley MT, Bowsher JE, Coleman RE. Improved lesion detection in SPECT using MLEM reconstruction. *IEEE Trans Nucl Sci* 1991;38:780-783.
12. Snyder DL, Miller MI. The use of sieves to stabilize images produced with the em algorithms for emission tomography. *IEEE Trans Nuclear Sci* 1985;NS-32:3864-3872.
13. Snyder DL, Miller MI, Thomas LJ Jr, Polite DG. Noise and edge artifacts in maximum-likelihood reconstruction for emission tomography. *IEEE Trans Med Imaging* 1987;MI-6:228-237.
14. Lange K. Convergence of EM image reconstruction algorithms with Gibbs smoothing. *IEEE Trans Med Imaging* 1990;9:439-446.
15. Nunez J, Llacer J. A fast Bayesian reconstruction algorithm for emission tomography with entropy prior converging to feasible images. *IEEE Trans Med Imaging* 1990;9:159-171.
16. Lalush DS, Tsui BMW. A new Gibbs prior for maximum a posteriori reconstruction in SPECT [Abstract]. *J Nucl Med* 1991;32:936.
17. Tsui BMW, Zhao XD, Lalush DS, Frey ED, Gullberg GT. Evaluation of iterative reconstruction methods for use in SPECT imaging [Abstract]. *J Nucl Med* 1991;32:937.
18. Miller TR, Sampathkumaran KS. Digital filtering in nuclear medicine. *J Nucl Med* 1982;23:66-72.
19. Sorenson JA, Phelps ME. *Physics in nuclear medicine*, second edition. Orlando: Grune and Stratton, Inc.; 1987:331-344, 408-419, 435-437, 560.
20. Hoffman EJ, Ricci AR, van der Stee M, Phelps ME. ECAT III—basic design considerations. *IEEE Trans Nucl Sci* 1983;NS-30:729-733.
21. Miller TR, Wallis JW. Fast maximum-likelihood reconstruction. *J Nucl Med* 1992;33:1710-1711.
22. King MA, Ljungberg M, Hademenos G, Glick SJ. A dual photopeak window method for scatter correction [Abstract]. *J Nucl Med* 1991;32:917.
23. Miller MI, Roysam B. Bayesian image reconstruction for emission tomography incorporating Good's roughness prior on massively parallel processors. *Proc Natl Acad Sci* 1991;88:3223-3227.
24. Butler CS, Miller MI. Maximum a posteriori estimation for SPECT using regularization techniques on massively-parallel computers. 1991 IEEE Nuclear Science Symposium and Medical Imaging Conference, Santa Fe, NM, 1991:2001-2005.
25. McCarthy AW, Miller MI. Maximum-likelihood SPECT in clinical computation times using mesh-connected parallel computers. *IEEE Trans Nucl Sci* 1991;38:426-436.
26. Kaufman L. Implementing and accelerating the EM algorithm for positron emission tomography. *IEEE Trans Med Imaging* 1987;MI-6:37-51.
27. Rajeevan N, Penney BC, Byrne C. An accelerated 3D maximum likelihood SPECT reconstruction. 1991 IEEE Nuclear Science Symposium and Medical Imaging Conference, Santa Fe, NM, 1991:1963-1968.

(continued from page 1668)

## SELF-STUDY TEST

# Gastrointestinal Nuclear Medicine

### ANSWERS

slowly over a 1-3 min duration. Presumably, this is due to spasm of the cystic duct, which impairs emptying of the gallbladder and falsely lowers the gallbladder ejection fraction.

#### References

1. Pickleman J, Peiss RL, Henkin R, et al. The role of sincalide cholescintigraphy in the evaluation of patients with acalculous gallbladder disease. *Arch Surg* 1985;120:693-697.
2. DeRidder P, Fink-Bennett D. The dilated common duct sign. A potential indicator of sphincter of Oddi dyskinesia. *Clin Nucl Med* 1984;9:262-263.

#### ITEMS 10-12: Properties of CCK

ANSWERS: 10, T; 11, F; 12, F

Cholecystokinin (CCK) is a 33-amino-acid polypeptide hormone produced by the duodenal mucosa in response to fat, lipolytic products, amino acids and small polypeptides in the small intestine. It causes the gallbladder to contract, the sphincter of Oddi to relax, enhances jejunal, ileal and, to a lesser extent, colonic motility, increases pyloric tone, and stimulates the secretion of pancreatic enzymes and bile. The diffuse effects of CCK on intestinal motility explain why many patients report "gurgling in the stomach" following its injection. Its active or cholecystokinetic portion resides totally in its C-terminal octapeptide fragment.

There are two commercial preparations of the 33-amino-acid polypeptide cholecystokinin: Pancreozymin™ is produced by Boots Co., Ltd., England, and Cholecystokinin™ by the Karolinska Institute in Stockholm. Both sincalide, the C-terminal octapeptide, and ceruletide diethylamine, the C-terminal decapeptide of cholecystokinin, are synthetic cholecystogogues. Sincalide (Kinevac™) is produced by Squibb & Sons, Inc., and ceruletide diethylamine (Tymtran™) by Adria Laboratories. Their effects on the gastrointestinal and hepatobiliary system are identical to that of intact cholecystokinin.

#### References

1. Fink-Bennett D. The role of cholecystogogues in the evaluation of biliary tract disorders. In: Freeman LM, Weissmann HS, eds. *Nuclear Medicine Annual* 1985. New York: Raven Press; 1985:107-132.

#### ITEMS 13-16 and 17-20: False-Positive Scintigraphy for Acute Cholecystitis

ANSWERS: 13, T; 14, T; 15, F; 16, T; 17, T; 18, T; 19, T; 20, F

The images in Figure 1 reveal rapid uptake of the radiotracer by the liver. The intrahepatic and extrahepatic ducts are seen by 15 min. By 30 min, there is transit of the radiotracer into the duodenal sweep. However, the gallbladder is not visualized throughout the 60 min of the study. Hence, there may be complete cystic duct obstruction (acute cholecystitis). Since the study was carried out only to 60 min, one cannot ascertain whether the gallbladder may eventually visualize (e.g., only chronic cholecystitis

may be present).

Among the causes of false-positive studies (i.e., nonvisualization of the gallbladder not due to cystic duct obstruction) are an insufficient period of fasting and acute pancreatitis. As many as 50% of normal individuals who are not fasted have nonvisualization of the gallbladder. Endogenous release of cholecystokinin and contraction of the gallbladder following a meal are presumed to prevent gallbladder filling. A fast of at least 2 hr, and preferably 4 hr, is required before beginning cholecystigraphy to minimize the effect of endogenous cholecystokinin. Prolonged fasting, for several days or more, such as may be encountered in post-operative patients or those receiving total parenteral feeding, also may lead to a false-positive cholecystigraphic study, presumably because the bile within the gallbladder is very viscous or mixed with sludge. Under such circumstances, it is helpful to administer cholecystokinin 30-60 min before cholecystigraphy; this will cause contraction of a normal gallbladder, which will then be in its refilling phase during the imaging study. It is generally agreed that acute pancreatitis may be a cause of nonvisualization of the gallbladder, although controversy exists as to the percentage of individuals with acute pancreatitis who will not have visualization of the gallbladder.

Since nonvisualization of the gallbladder at 60 min may be due to chronic cholecystitis as well as acute cholecystitis, several approaches have been developed to distinguish between them. Obtaining images up to 4 hr postinjection has been shown by many investigators to be useful in separating chronic cholecystitis from acute cholecystitis. The gallbladder will eventually visualize in patients with chronic cholecystitis since the cystic duct is patent, although the gallbladder may be scarred and sluggish. In patients with acute cholecystitis, the cystic duct is virtually always functionally or anatomically obstructed, and the gallbladder will not visualize.

The false-positive rate for acute cholecystitis also can be reduced significantly by medicating the patient with a cholecystokinin analogue, or by use of morphine sulfate. Cholecystokinin given intravenously (slowly over 1-3 min) empties a sludge-filled or distended gallbladder, allowing a second dose of the hepatobiliary agent to flow into the gallbladder. If the cystic duct is obstructed, the gallbladder cannot contract against the obstruction. Alternately, if the gallbladder fails to visualize by 1 hr, 0.04 mg/kg morphine sulfate diluted in 10 ml of saline may be given intravenously with further imaging over the next 30 min. Morphine increases the tone of the sphincter of Oddi at the distal common bile duct. The resultant increase in pressure within the biliary system is enough to overcome a partial obstruction of the cystic duct, or to cause filling of a fibrosed gallbladder, thus bringing about earlier visualization of the gallbladder.

(continued on page 1695)